Faraday Discussions
Cite this: DOI: 10.1039/d5fd00135h

PAPER

View Article Online
View Journal

Ionic memory or electrode artefacts? A systematic assessment of nanofluidic memristors

Siddhi Vinayak Pandey, [ac] Kalluvadi Veetil Saurav, [bc] Solleti Goutham, [ac] Anshu Sharma, [ad] Ashok Keerthi [bc] and Boya Radha *[ac]

Received 30th November 2025, Accepted 29th January 2026
DOI: 10.1039/d5fd00135h

Nanofluidic memristors have recently emerged as a promising alternative to mimic brain-like synaptic functions for neuromorphic applications. Here, we observed that when fluidic devices such as nanoporous membranes are measured with Ag/AgCl electrodes, pinched hysteresis in current–voltage (I–V) loops can be generated even when there is no intrinsic ionic memory behaviour. The nanoporous membranes like nitrocellulose/mixed-cellulose ester (MCE) and polyvinylidene fluoride (PVDF) show memory signatures including pinched I–V loops, nonlinearity, and frequency dependent variation in loop area with Ag/AgCl electrodes, whereas the I–V response became purely capacitive when platinum or glassy carbon electrodes were used in two/three-electrode configurations. The same hysteresis could also be reproduced in a bulk electrolyte without any membrane, confirming its origin due to the Ag $\rightleftharpoons$ AgCl redox reaction and salt deposition. In contrast, nanochannel devices made by van der Waals assembly of 2D materials retained their characteristic memory loops regardless of the chosen electrode material. These results show that electrode effect can mimic fundamental memristive signatures and therefore highlight the importance of electrode control to develop reliable, energy efficient fluidic computing architectures.

1. Introduction

Memristors proposed by Chua have attracted wide interest for their potential to emulate the adaptive learning behaviour of the biological brain.[1] They are now central to neuromorphic and bioinspired computing, as they offer tunable history

[a]Department of Physics and Astronomy, School of Natural Sciences, The University of Manchester, Manchester M13 9PL, UK. E-mail: radha.boya@manchester.ac.uk
[b]Department of Chemistry, School of Natural Sciences, The University of Manchester, Manchester M13 9PL, UK
[c]National Graphene Institute & Photon Science Institute, The University of Manchester, Manchester M13 9PL, UK
[d]Department of Applied Sciences and Humanities, Central University of Haryana, Mahendragarh 123029, Haryana, India

dependent resistance along with volatile and non-volatile memory states.[2–4] Most demonstrations of memristors in the past decade were solid-state and relied on electronic transport such as carrier drift or electric field-driven redox processes following the first experimental demonstration[5] in 2008. Biological synapses work with the flow of ions through selective nanochannels.[6] Nanofluidic devices mimic this *via* selective ion transport through confined nanochannels, where the applied voltage stimuli can produce history dependent conductance changes analogous to synaptic weight modulation.[7–12]

In nanofluidic memristor measurements, a two-electrode arrangement is commonly used, with a separate working electrode and a combined counter/reference electrode. Ag/AgCl electrodes are often employed in such two-electrode systems as they provide a stable potential and exhibit low polarization in chloride based electrolytes.[13] However, in chloride rich environments, these electrodes are not chemically inert as the AgCl can dissolve to form silver–chloride complexes. Moreover, the Ag^+ can also migrate through the electrolyte, and metallic silver can redeposit on the opposite electrode. These coupled (Ag $\rightleftharpoons$ AgCl) redox and film growth processes can cause additional charge-transfer pathways that overlay the intrinsic device response.[14]

Confirmation of memristive behavior in *I–V* characteristics is commonly based on three fingerprints as described by Chua, which are pinched hysteresis at the origin, frequency dependent loop area, and the pinched hysteresis loop shrinkage to a single valued function at infinite frequency.[4] In nanofluidic systems, these features can arise through two fundamentally different mechanisms. The first is intrinsic channel memristance, where strongly confined geometries show voltage driven ionic rearrangement and interfacial charge modulation.[15–19] This mechanism produces a stable ionic conductance state that remains unchanged regardless of the electrode material. The second is electrode dominated redox hysteresis that originates from electrochemical reactions at reactive electrodes.[14] Disentangling intrinsic and extrinsic phenomena in nanofluidic channels that drive hysteresis is therefore critical for identifying and programming ionic memory. In this work, we make this separation explicit by investigating *I–V* characteristics of several fluidic systems including porous membranes, and van der Waals nanochannels with several electrode materials such as Ag/AgCl, Pt and glassy carbon. Our results show that the choice is central to interpreting nanofluidic memristors, as it provides a direct means to test whether a memory-like *I–V* loop is intrinsic to the device or instead arises from electrochemical artefacts.

2. Methods

2.1. Devices

We utilised two commercially available nanoporous membranes for ionic memory measurements. The first was a nitrocellulose/mixed cellulose ester (MCE) membrane (from Merck Millipore, MF-Millipore™, REF VSWP02500) with ~25 mm diameter discs, hydrophilic and non-sterile characteristics, with a 25 nm pore size. The second was a polyvinylidene fluoride (PVDF) membrane (from Merck Millipore, REF VVLP04700), supplied as 47 mm discs, hydrophilic and non-sterile characteristics, with a 100 nm pore size. We have also fabricated a micro-hole (~3 × 25 μm) on a silicon nitride chip, and van der Waals 2D nanochannel devices on free standing silicon nitride (SiN_x) membranes.[20,21] The micro-hole

structure was patterned on SiN_x/Si membranes using standard photolithography and reactive ion etching techniques. For nanochannels, mechanically exfoliated hexagonal boron nitride (hBN) flakes were used as the top and bottom encapsulation layers, with few layer graphene as the channel spacer. Graphene spacers were patterned by electron beam lithography followed by oxygen plasma etching to define channel width (~130 nm). The top/spacer/bottom vdW heterostructures were stacked covering a microhole ~3 × 25 μm on a free standing Si/SiN_x membrane (SI Fig. 1). The assembled heterostructures on the membrane were subsequently annealed at 300 °C for 3 hours and 400 °C for 4 hours in a 10% H_2/Ar atmosphere to remove residues and strengthen interlayer adhesion. Then the channel length was defined with a gold patch patterned on the heterostructure by lithography, deposition, and dry etching (SI Fig. 2).

2.2. Measurements

Electrochemical measurements were performed using a custom-built fluidic cell, where the membrane/device separated two-electrolyte reservoirs filled with aqueous salt solutions. Before the first *I–V* measurement, fresh PVDF or MCE membranes were rinsed with deionised water until they were fully wet. The wet membrane was then gently placed in the fluidic cell. The measurements were carried out for mono, bi, and trivalent electrolytes including KCl, HCl, $CaCl_2$, $MnCl_2$, $AlCl_3$ with concentrations varying from 1 μM to 3 M. The electrical response was recorded in either two or three-electrode configuration using a Biologic SP-300 electrochemical workstation. The Ag/AgCl electrodes were prepared by immersing high purity silver rod overnight in sodium hypochlorite solution to form a uniform silver chloride layer. For comparison, commercially available Ag/AgCl, platinum and glassy carbon electrodes were also used. Electrodes were immersed on both sides of the device within the fluidic chamber. Measurements were conducted in a grounded Faraday cage to minimize electrical interference and ensure a stable *I–V* response.

2.3. Characterization

The atomic force microscopy (AFM) images of the graphene spacer were obtained using a Dimension FastScan (Bruker, USA) instrument in tapping mode. Comprehensive structural and surface characterization was performed to elucidate the morphology of the devices and electrodes. Field Emission Scanning electron microscopy (FE-SEM) from Zeiss ULTRA 55, with 5 kV accelerating voltage was used to visualize the structure of Ag/AgCl electrodes. Energy dispersive X-ray spectroscopy (EDX) confirmed the successful formation of the AgCl layer on the lab-made silver electrodes. Quantitative determination of the composition of the deposited silver containing compounds is challenging because several characteristic X-ray lines overlap. For example, Ag exhibits Lα and related L-series peaks at approximately 0.312 keV and 2.634–3.151 keV, whereas Cl shows its Kα and Kβ lines at around 2.622 keV and 2.816 keV and K shows its Kα and Kβ lines near 3.314 keV and 3.590 keV. The proximity of these Lα and Kα emissions leads to substantial spectral overlap, complicating accurate quantitative analysis. SEM imaging of the PVDF and MCE membranes was performed at an accelerating voltage of 3 kV. Prior to imaging, a 10 nm gold layer was deposited on the PVDF membrane to minimize surface charging.

3. Results and discussion

We analysed the electrochemical response of the nanoporous membranes and nanochannel devices from the measurements in two-electrode (Ag/AgCl) configuration with aqueous electrolytes. The measurement configuration, illustrated in Fig. 1a, consists of a two-electrode setup where both electrodes are immersed in the electrolyte, and the device is positioned inbetween the electrolyte reservoirs. A voltage stimulus was applied to drive ionic transport across the device, and the corresponding current was recorded.

Fig. 1b–d shows the *I–V* characteristics of various different device architectures. The porous membranes of PVDF (effective pore size, 100 nm) and MCE (effective pore size, 25 nm) have shown hysteretic loops that are pinched at the origin (Fig. 1b and c). We have also varied the frequency, salt type, and its concentration (SI Fig. 3) with PVDF membranes to track how the hysteresis evolves. With both membranes, the direction of the loops was clockwise, and such hysteresis loops observed previously with 2D nanochannels were attributed to ion

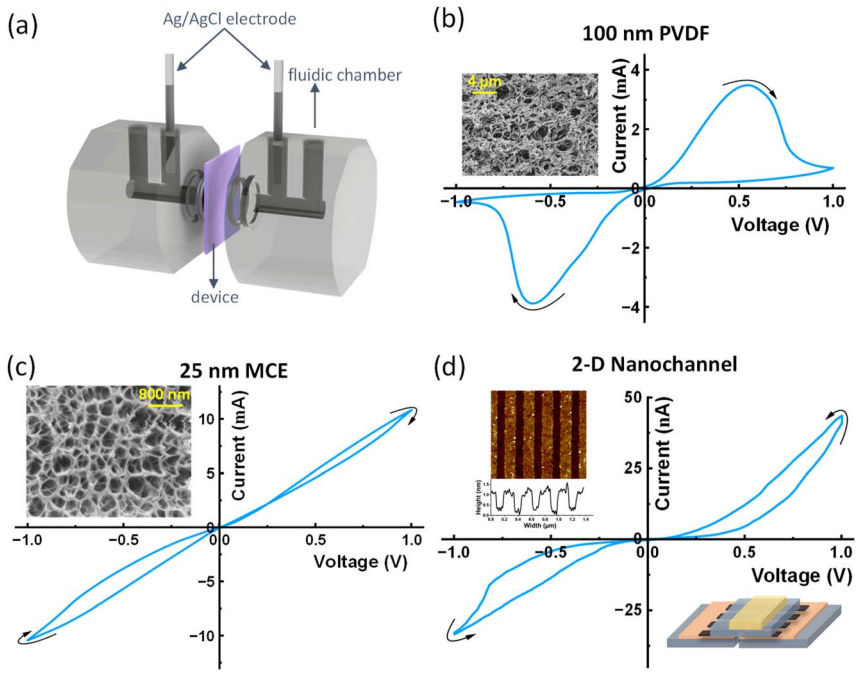

Fig. 1 Schematic and electrical characterization of ion transport devices measured using a two-electrode Ag/AgCl configuration within a ±1 V potential window in 1 M KCl. (a) Schematic of the experimental setup showing the fluidic chamber and device configuration. (b) *I–V* characteristics of a 100 nm PVDF membrane, with the inset showing the membrane surface morphology. (c) *I–V* characteristics of a 25 nm MCE membrane, with the inset showing an SEM image of the porous structure. (d) *I–V* characteristics of the bi-layer nanofluidic channel fabricated by sandwiching a graphene spacer between top and bottom hBN flakes, with the inset showing an AFM image and height profile of the graphene spacer along with a schematic of the 2D device. All measurements were performed at 3.75 mHz, except for the bi-layer nanochannel tested at 8.33 mHz sweep frequency.

concentration polarization leading to current saturation.[22] Both the PVDF and MCE membranes produced relatively large current (in the milliampere range), which is substantially higher than the typical nanoampere level currents observed in nanofluidic devices. The insets in both figures show the SEM images of the membranes, showing the interconnected porous structure. Many of these surface pores are much larger than the sizes mentioned in the commercial membranes, however the effective pore size for the whole thickness of the membrane is reported as measured from the manufacturer to be around 100 nm for PVDF and 25 nm for MCE. Further measurements with a micro-hole (3 μm × 25 μm dimension) as shown in SI Fig. 1 provided a linear *I*–*V* response without any pinching, and hysteresis. This purely ohmic behaviour indicates the absence of memristive effects.[1,4,23]

The nanochannels fabricated by van der Waals assembly (Fig. 1d), with a graphene spacer confined between top and bottom hBN flakes (SI Fig. 2), show an *I*–*V* loop with an anticlockwise direction with hysteresis and clear pinching at the origin. Such loops are attributed to ion dissociation–association dynamics due to the Wien effect under the applied voltage, and the kinetics of this phenomenon leads to hysteresis and ionic memory in nanoconfined systems. Several confined nanofluidic architectures displaying such hysteresis loops in the literature[8,16,24–27] have demonstrated neuromorphic properties.

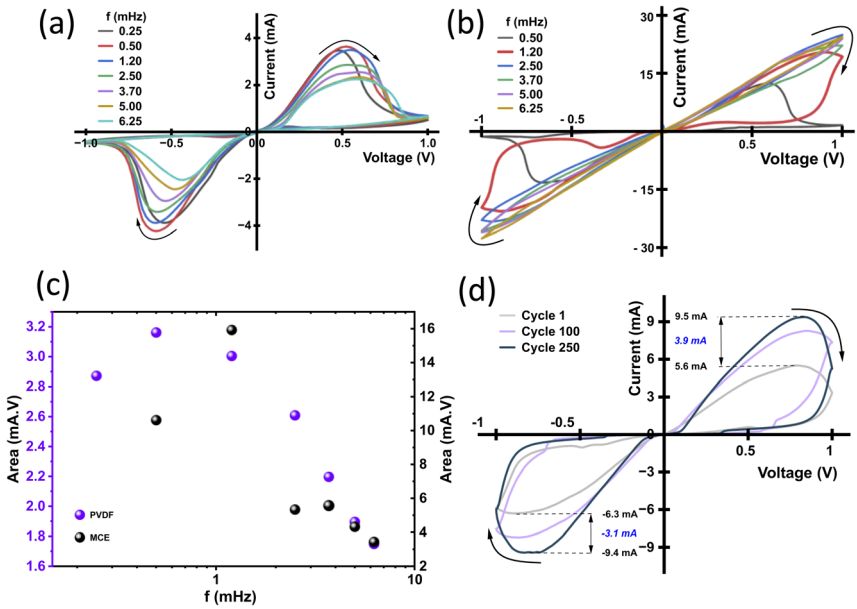

Fig. 2 *I*–*V* characteristics of membranes. *I*–*V* characteristics of (a) 100 nm PVDF membrane in 1 M KCl at frequencies from 0.25 to 6.25 mHz, and (b) 25 nm MCE membrane in 1 M HCl at frequencies from 0.50 to 6.25 mHz. (c) Variation of the enclosed *I*–*V* loop area with frequency for the PVDF and MCE membranes shown in (a) and (b). (d) Cyclic *I*–*V* response of the 100 nm PVDF membrane in 1 M KCl, showing an increase in current from approximately 3.1 mA (in negative potential window) to 3.9 mA (in positive potential window) between the 1st and 250th cycles.

A nanochannel device with a bi-layer graphene spacer shows intrinsic ionic memory with Ag/AgCl electrodes, as has been previously reported.[7,22] As the PVDF and MCE membranes also display pinched hysteresis loops, we do a closer examination of the underlying mechanisms by varying frequency (Fig. 2a and b) and performing endurance cycling (Fig. 2d). For the 100 nm PVDF membrane in 1 M KCl (±1 V), the loop area increased from 0.25 to 1.2 mHz and then decreased up to 6.25 mHz (Fig. 2c). This shows a strong frequency dependency. Similarly, the same trend has also been observed with the 25 nm MCE membrane in 1 M HCl (Fig. 2b). Furthermore, we performed endurance tests on the PVDF membrane with Ag/AgCl electrodes up to 250 cycles, where the current magnitude at ±1 V evolved from +5.6/−6.3 mA (cycle 1) to +9.5/−9.4 mA (cycle 250) (Fig. 2d). Taken together, these pinched loops, frequency dependent area, and cycle dependent conductance suggest these porous membranes show the hallmark features of memory-like behaviour.

We next examined the electrode surfaces using FE-SEM and EDX mapping (Fig. 3). These measurements reveal cycling induced morphological and compositional changes at the Ag/AgCl electrodes, consistent with the pronounced whitening of the electrode surface observed after cycling (SI Fig. 5).

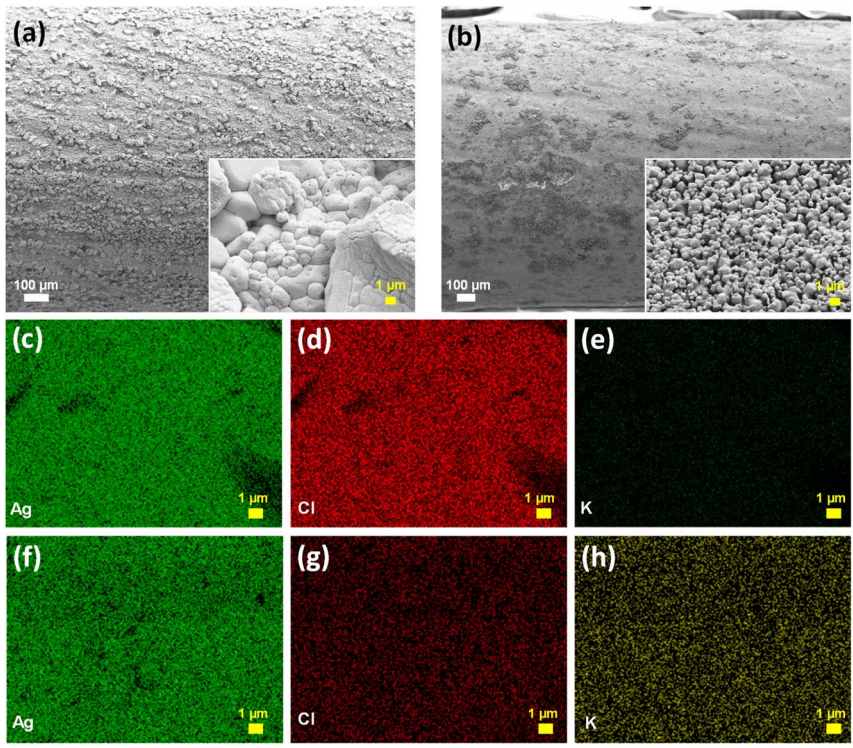

Fig. 3 SEM and EDX images of electrodes before and after cycling. SEM images of the (a) fresh Ag/AgCl electrode, and (b) electrode after 250 cycles, acquired at 5 kV. (c–e) EDX elemental maps of the fresh electrode for silver (Ag), chlorine (Cl), and potassium (K). (f–h) EDX elemental maps of the electrode after 250 cycles.

In Fig. 3a, the freshly prepared electrode shows both the Ag and AgCl layer. After 250 *I–V* cycles in 1 M KCl (Fig. 3b), the surface becomes visibly rough (SI Fig. 5) and is covered with granular, clustered deposits. These features are in line with previous reports[28,29] which suggests that AgCl films undergo cracking and partial regrowth during electrochemical operation. Correspondingly, the EDX elemental maps in Fig. 3c–e show that the fresh electrode contains only silver (Ag) and chlorine (Cl), with no detectable potassium (K). After 250 cycles, the Ag and Cl maps in Fig. 3f–h appear less uniform, consistent with surface changes seen in Fig. 3b. The K map in Fig. 3h shows an elemental map of the cycled electrode, confirming K^+ trapping from KCl electrolyte. Previous work on AgCl electrodes has shown that external ions can be trapped in the AgCl layer when the film becomes porous or locally disrupted during electrochemical use. This allows ion movement along grain boundaries and through surface pores or microchannels.[28]

The Ag/AgCl electrodes could undergo significant restructuring under repeated bias. Cycling-induced modifications to the AgCl layer, including crack formation, partial regrowth, and local salt deposition, changes the interfacial composition and can influence the electrode's redox response.[29,30] This supports the view that the hysteresis observed in our *I–V* measurements originates from electrode–electrolyte interactions rather than from any intrinsic memristive behaviour of the membrane. Such cycling-induced electrode modifications are observed only in the high-current membrane measurements. For vdW nanochannel devices, the *I–V* cycling followed by optical imaging (SI Fig. 5c and d) and SEM/EDX analysis (SI Fig. 6) show no visible colour change, surface roughening of the Ag/AgCl electrodes, consistent with operation in the nanoampere current regime.

To isolate any electrode contribution and considering the high current typically observed with the PVDF and MCE membranes, we varied both the electrode material and the measurement configuration between two and three-electrode systems (Fig. 4a). We examined the effect of changing the electrode material in the two-electrode system (Fig. 4b). When Ag/AgCl was replaced with inert glassy carbon or platinum, the PVDF membrane showed a capacitive type loop without any pinching. This observation prompted a key question, whether the previously observed *I–V* hysteresis arises from the PVDF membrane itself or merely from electrochemical processes at the electrode–electrolyte interface? To resolve this, we performed a control experiment with Ag/AgCl electrodes under identical conditions. One *I–V* was recorded with the PVDF membrane and another with only bulk electrolyte in the cell (without any membrane). As shown in Fig. 4d, both traces show similar pinched hysteresis and redox-like features, indicating that the response is dominated by interfacial Ag $\rightleftharpoons$ AgCl chemistry with plausible reaction involving $AgCl(s) + Cl^- \rightleftharpoons [AgCl_2^-](aq)$, $AgCl(s) + e^- \rightleftharpoons Ag(s) + Cl^-$ and $AgCl_2^-(aq) + e^- \rightleftharpoons AgCl(s) + 2Cl^-$ and electrode polarization rather than ionic transport through the porous membranes. In chloride rich electrolytes, Ag/AgCl electrodes can be electrochemically active. During cyclic voltammetry, the Ag/AgCl surface could take part in reversible redox processes. Under applied bias, AgCl might undergo oxidative dissolution to form soluble chloro complexes such as $[AgCl_2]^-$, $[AgCl_3]^{2-}$, $[AgCl_4]^{3-}$ or other silver containing compounds such as Ag_2O which would increase the number of mobile charge carriers. As a result, the current increase on both positive and negative sweeps reflects a reversible electrochemical activity of the electrode (Fig. 2d). Dissolution and complexation of the

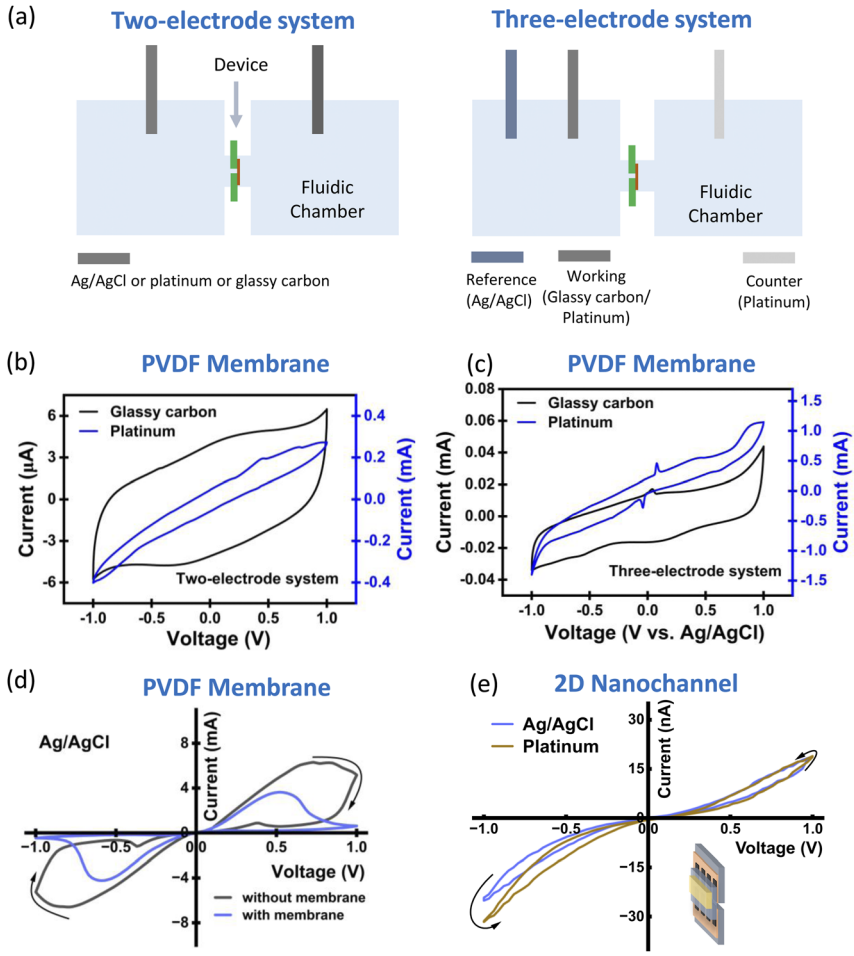

Fig. 4 Effect of electrode configuration and material on *I*–*V* characteristics. (a) Schematic of two- and three-electrode configurations. In three-electrode system, a commercial Ag/AgCl reference electrode is used as the reference, platinum as the counter, and either glassy carbon or platinum as the working electrode. In case of the two-electrode system, identical electrodes of either Ag/AgCl or platinum (see Methods) been used. (b) *I*–*V* response of a 100 nm PVDF membrane measured in the two-electrode configuration using platinum and glassy carbon electrodes. (c) *I*–*V* characteristics of a 100 nm PVDF membrane measured in the three-electrode system using either glassy carbon or platinum as working electrode. (d) Comparison of *I*–*V* response with and without PVDF membrane using Ag/AgCl electrodes. (e) *I*–*V* characteristics of a 2D nanochannel measured in the two-electrode configuration using platinum and Ag/AgCl electrodes. All measurements were performed in 1 M KCl within a ±1 V potential window.

AgCl layer during voltage sweeps generate a history dependent interfacial conductance, which gives rise to the observed memristor-like hysteresis even in bulk electrolyte without a membrane (Fig. 4d).

We then tested whether the measurement configuration plays any role by switching to a three-electrode configuration (Fig. 4a). Here, we used a commercial Ag/AgCl reference electrode, platinum as the counter, and alternated the working

electrode between glassy carbon and platinum. In 1 M KCl within ±1 V, the PVDF membrane showed no pinching in *I–V* but only capacitive behaviour (Fig. 4c). The memristor-like loops appear only when Ag/AgCl itself participates in current flow, confirming that they originate from Ag ⇌ AgCl electrochemistry.

To distinguish electrode driven effects from intrinsic ionic memory behaviour, a van der Waals nanochannel with a bi-layer graphene spacer (see Methods) was also tested in 1 M KCl using Ag/AgCl and Pt electrodes. The *I–V* response was independent of electrode material (Fig. 4e). In this case, the nanochannel acts as a high-resistance element that limits the current magnitudes and the response arises solely from the confined geometry rather than any electrode based redox activity. In contrast, PVDF and MCE membranes exhibit clockwise *I–V* loops milliampere (mA) scale current characteristic to saturation type redox polarization at the electrode–electrolyte interface. The persistence of similar current magnitudes despite changes in electrolyte type and concentration (SI Fig. 3) indicates that the response is dominated by electrode processes rather than by membrane or electrolyte properties. This behaviour reflects the low effective resistance of porous membranes, where many parallel ionic pathways make the device resistance comparable to that of the bulk electrolyte and electrode–electrolyte interfaces, so that these contributions dominate the measured response. Accordingly, clockwise loops with high current levels should be regarded as electrode-dominated unless confirmed by inert-electrode and electrolyte-only control measurements.

The memory-like signatures in porous membranes thus originate solely due to electrode–electrolyte interactions and deposition. We examined whether such interfacial processes can also mimic synaptic behavior. To explore this, standard neuromorphic measurements including potentiation, depression, retention, and endurance were performed using the PVDF membrane in 1 M KCl solution with Ag/AgCl electrodes (Fig. 5a–d).

In an ideal potentiation process, conductance should increase with successive write pulses, reflecting synaptic weight strengthening. In the membranes, however, the conductance rapidly decreases and saturates within two pulses (Fig. 5a), with no incremental growth. This behaviour is inconsistent with potentiation and instead suggests a transient, non-programmable response, likely linked to AgCl formation at the Ag/AgCl electrode. Similar monotonic decay is observed during depression (Fig. 5b), and the system does not show any clear separation or adaptive evolution between potentiation and depression, indicating that it does not reliably store or update an internal state. In the retention measurement (Fig. 5c), slow conductance decay at a small read bias (0.1 V) could superficially resemble short term memory, but in an electrochemical context it is more naturally attributed to relaxation of the electrode–electrolyte interface specifically, the decaying nature could be due to interfacial polarization and dissolution of residual AgCl after bias removal. The endurance data (Fig. 5d) also show distinct high/low states only for the first ~15 cycles, after which both states converge as the Ag/AgCl interface approaches electrochemical equilibrium. So although the on–off states look distinct with good ratio in the beginning cycles (as also reported in ref. 14) such electrochemical hysterisis soon merges on and off states with repeated cycling, and tends to be unreliable.

Overall, the consistently decreasing conductance trends in potentiation, depression, and retention, are best understood as relaxation dynamics of the Ag/

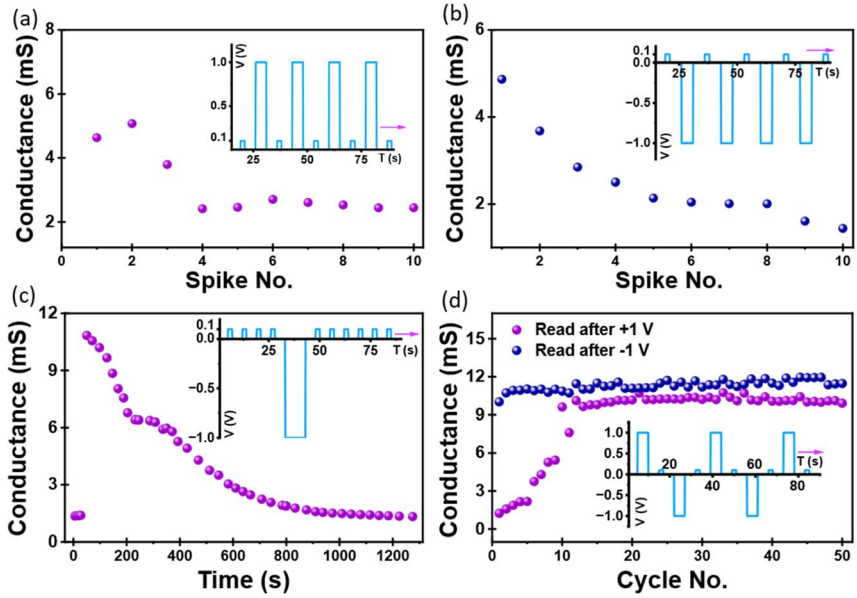

Fig. 5 Neuromorphic characterization with PVDF membrane. (a) Potentiation: the conductance evolution recorded at a 0.1 V (1 s) read following successive +1 V (5 s) write pulses. (b) Depression: conductance decay measured at 0.1 V (2 s) read after repeated −1 V (5 s) erase pulses, showing a consistent decrease similar to conventional depression behaviour. (c) Retention characteristics obtained by reading the device at 0.1 V (1 s) to establish the initial state, next a −1 V (10 s) write signal is applied to continuously observe the device conductance state at 0.1 V. (d) Endurance is recorded by successively applying +1 V (5 s) write and −1 V (5 s) erase pulses with 0.1 V (2 s) read after each. Between each pulse, relaxation with 0 V has been applied for 5 s. All measurements were carried out in a two-electrode Ag/AgCl configuration with 1 M KCl solution. In the voltage–time insets of all figures, only a representative time window is shown for clarity, while the purple arrows indicate that the same input protocol is continuously applied beyond the displayed region over the full measurement duration.

AgCl electrode–electrolyte interface. While these decays can mimic signatures of short term (volatile) memory at the measurement level, they do not reflect programmable synaptic states.

4. Conclusions

We systematically tested a wide range of ion transport systems including micro-hole, porous membranes, and 2D-nanochannels to distinguish intrinsic device driven memory from electrode-induced artefacts. The micro-hole showed linear and symmetric *I–V* responses, confirming the absence of memristive behaviour. In contrast, the PVDF and MCE membranes displayed fingerprints of Chua's signature of memory, *i.e.*, hysteresis pinching at the origin, and frequency dependent area, yet their apparent memory signature vanished when the Ag/AgCl electrodes were replaced with inert Pt or glassy carbon electrodes in two/three-electrode configurations. These results confirm that the observed hysteresis

originates from Ag ⇌ AgCl interfacial processes rather than any intrinsic modulation within the membranes.

For a device that shows memristive nature, its *I–V* response should remain independent of electrode material. The 2D nanochannels show stable and reproducible loops with low current magnitude (nA range) for both Pt and Ag/AgCl electrodes which clarifies that the memory arises through confinement. Unlike this, the porous membrane shows high current (mA range), with saturation type clockwise loops that depend strongly on electrode material and thus represent electrode driven redox polarization.

These findings highlight a simple diagnostic for fluidic memristors. Saturation type hysteresis with large current in aqueous systems should first be checked for an electrode contribution rather than assumed to be an intrinsic device property. A simple way to verify this is to repeat the measurement with an inert electrode under the same conditions, if the loop disappears or changes shape, the effect is electrode driven. This simple control helps prevent electrode artefacts from being misinterpreted as fluidic memristive behavior and supports the development of reliable neuromorphic and nanofluidic architectures for brain-like computing.

Author contributions

B. R. designed and directed the project. S. V. P. performed all the electrochemical measurements and led data analysis with input from B. R. K. V. S. carried out SEM and EDX of Ag/AgCl electrodes and membranes and fabricated the micro-hole and nanochannel device. S. G. initially observed the hysteresis loops with PVDF. A. S. reproduced measurements with PVDF membranes. S. V. P. and B. R. wrote the manuscript with inputs from K. V. S. and A. K. All authors contributed to the discussions.

Conflicts of interest

The authors declare no competing interests.

Data availability

The data supporting the findings of this study are openly available on Figshare at https://doi.org/10.6084/m9.figshare.31801786.

Supplementary information (SI): additional *I–V* measurements across different electrolytes and frequencies, fabrication schematics of nanochannels, and SEM/EDX characterization of electrodes before and after cycling. See DOI: https://doi.org/10.1039/d5fd00135h.

Acknowledgements

B. R. acknowledges funding from the Royal Society University Research Fellowship (URF\R\231008), the Philip Leverhulme Prize (PLP-2021-262), the European Union's H2020 Framework Programme/ERC Starting Grant 852674 – AngstroCAP, and the EPSRC New Horizons Grant (EP/X019225/1). A. K. acknowledges EPSRC New Horizons Grant (EP/V048112/1). B. R. and A. K. also acknowledge EPSRC Strategic Equipment Grant (EP/W006502/1). S. V. P. acknowledges support from

Deans Doctoral Scholarship (DDS). A. S. acknowledges Science and Engineering Research Board (SERB), and Department of Science and Technology (DST) for International Research Experience (SIRE) grant (SIR/2022/001589). S. V. P. thanks S. Rahaman from the Angstrofluidics group of University of Manchester and Dr A. Ismail from Université Paris Saclay for helpful discussions.

References

1 L. Chua, Memristor-the missing circuit element, *IEEE Trans. Circuit Theory*, 1971, **18**, 507–519.
2 Y. Zhang, *et al.*, A system hierarchy for brain-inspired computing, *Nature*, 2020, **586**, 378–384.
3 G. Kreiman, C. Koch and I. Fried, Imagery neurons in the human brain, *Nature*, 2000, **408**, 357–361.
4 L. Chua, If it's pinched it's a memristor, *Semicond. Sci. Technol.*, 2014, **29**, 104001.
5 D. B. Strukov, G. S. Snider, D. R. Stewart and R. S. Williams, The missing memristor found, *Nature*, 2008, **453**, 80–83.
6 T.-H. Lee, *et al.*, Synaptic plasticity and metaplasticity of biological synapse realized in a $KNbO_3$ memristor for application to artificial synapse, *ACS Appl. Mater. Interfaces*, 2018, **10**, 25673–25682.
7 P. Robin, *et al.*, Long-term memory and synapse-like dynamics in two-dimensional nanofluidic channels, *Science*, 2023, **379**, 161–167.
8 T. Xiong, *et al.*, Neuromorphic functions with a polyelectrolyte-confined fluidic memristor, *Science*, 2023, **379**, 156–161.
9 Y. Bu, Z. Ahmed and L. Yobas, A nanofluidic memristor based on ion concentration polarization, *Analyst*, 2019, **144**, 7168–7172.
10 Y. Noh and A. Smolyanitsky, Synaptic-like plasticity in 2D nanofluidic memristor from competitive bicationic transport, *Sci. Adv.*, 2024, **10**, eadr1531.
11 G. Xu, *et al.*, Nanofluidic ionic memristors, *ACS Nano*, 2024, **18**, 19423–19442.
12 X. Zhou, *et al.*, Nanofluidic memristor based on the elastic deformation of nanopores with nanoparticle adsorption, *Natl. Sci. Rev.*, 2024, **11**, nwad216.
13 A. J. Bard, *Standard Potentials in Aqueous Solution*, Routledge, 2017.
14 S. Rafique, *et al.*, Aqueous Electrochemical Memristor Based on Reversible Insulating-Layer Dynamics Emulating Neuromorphic Functions, *ACS Appl. Mater. Interfaces*, 2025, **17**, 55597.
15 G. Laucirica, M. E. Toimil-Molares, W. A. Marmisollé and O. Azzaroni, Unlocking Nanoprecipitation: A Pathway to High Reversibility in Nanofluidic Memristors, *ACS Appl. Mater. Interfaces*, 2024, **16**, 58818–58826.
16 Y. Ling, *et al.*, Single-pore nanofluidic logic memristor with reconfigurable synaptic functions and designable combinations, *J. Am. Chem. Soc.*, 2024, **146**, 14558–14565.
17 S. Portillo, J. Cervera, S. Mafe and P. Ramirez, Reversible logic with a nanofluidic memristor, *Phys. Rev. E*, 2024, **110**, 065101.
18 S. Portillo, *et al.*, pH-Dependent Effects in Nanofluidic Memristors, *J. Phys. Chem. Lett.*, 2024, **15**, 7793–7798.
19 P. Ramirez, V. Gómez, J. Cervera, S. Mafe and J. Bisquert, Synaptical tunability of multipore nanofluidic memristors, *J. Phys. Chem. Lett.*, 2023, **14**, 10930–10934.

20 A. Bhardwaj, *et al.*, Fabrication of angstrom-scale two-dimensional channels for mass transport, *J. Phys. Chem. Lett.*, 2024, **19**, 240–280.
21 T. Mouterde, *et al.*, Molecular streaming and its voltage control in ångström-scale channels, *Nature*, 2019, **567**, 87–90.
22 A. Ismail, *et al.*, Programmable memristors with two-dimensional nanofluidic channels, *Nat. Commun.*, 2025, **16**, 7008.
23 L. O. Chua and S. M. Kang, Memristive devices and systems, *Proc. IEEE*, 1976, **64**, 209–223.
24 T. Emmerich, *et al.*, Nanofluidic logic with mechano–ionic memristive switches, *Nat. Electron.*, 2024, **7**, 271–278.
25 T. Emmerich, *et al.*, Nanofluidics, *Nat. Rev. Methods Primers*, 2024, **4**, 69.
26 K. Liu, *et al.*, Resistance-Restorable Nanofluidic Memristor and Neuromorphic Chip, *Nano Lett.*, 2025, **25**, 6530–6538.
27 G. Rivera-Sierra, P. Ramirez, J. Bisquert and A. Bou, Relaxation Time of Multipore Nanofluidic Memristors for Neuromorphic Applications, *J. Am. Chem. Soc.*, 2025, **147**, 17529–17538.
28 Z. Zhang, *et al.*, Relationship between microstructure of AgCl film and electrochemical behavior of Ag|AgCl electrode for chloride detection, *Corros. Sci.*, 2021, **184**, 109393.
29 X. Jin, J. Lu, P. Liu and H. Tong, The electrochemical formation and reduction of a thick AgCl deposition layer on a silver substrate, *J. Electroanal. Chem.*, 2003, **542**, 85–96.
30 H. Ha and J. Payer, The effect of silver chloride formation on the kinetics of silver dissolution in chloride solution, *Electrochim. Acta*, 2011, **56**, 2781–2791.